Operando spectroscopic observation of dynamic-coupling oxygen on single-atomic iridium catalyst for acidic water oxidation

Hui Su
University of Science and Technology of China
Wanlin Zhou
University of Science and Technology of China
Wu Zhou
Shihezi University
Yuanli Li
University of Science and Technology of China
Li Rong Zheng
Chinese Academy of Sciences
Hui Zhang
University of Science and Technology of China
Meihuan Liu
University of Science and Technology of China
Xiuxiu Zhang
University of Science and Technology of China
Xuan Sun
University of Science and Technology of China
Yanzhi Xu
University of Science and Technology of China
Fengchun Hu
University of Science & Technology of China
Jing Zhang
Institute of high energy physics, chinese academy of science
Tiandou Hu
Chinese Academy of Sciences
Qinghua Liu
University of Science and Technology of China https://orcid.org/0000-0003-4090-3311
Shiqiang Wei (sqwei@ustc.edu.cn)
University of Science and Technology of China https://orcid.org/0000-0002-2052-1132

Article

Keywords: acidic water oxidation, oxygen evolution reaction (OER) electrocatalysts, Operando spectroscopic observation

Posted Date: June 4th, 2021

DOI: https://doi.org/10.21203/rs.3.rs-568365/v1

Version of Record: A version of this preprint was published at Nature Communications on October 21st, 2021. See the published version at https://doi.org/10.1038/s41467-021-26416-3.

Abstract

Uncovering the dynamics of active sites under working state is crucial to realizing increased activity, enhanced stability and reduced cost of oxygen evolution reaction (OER) electrocatalysts in proton exchange membrane electrolytes. Herein, we identify at atomic level a potential-driven dynamic-coupling oxygen on the hetero-nitrogen configured single-atomic Ir sites (HN-Ir NC) during OER working conditions to successfully endow the single-atomic Ir catalyst with an ultrahigh electrochemical acidic-OER activity. Using *operando* synchrotron radiation infrared and X-ray absorption spectroscopies, we directly observe in the experiment that a dynamic oxygen atom is formed at the Ir site with the O-hetero-Ir-N_4 structure as more electrophilic active center and then effectively promote the generation of the key *OOH intermediates under working potentials, which is exceptionally favourable for the dissociation of H_2O over Ir sites and resistance to over-oxidation and dissolution of the active sites.The optimal single-atomic HN-Ir NC catalyst delivers a large mass activity of 2860 A g_{metal}^{-1} and a huge turnover frequency of 5110 h^{-1} at a low overpotential of 216 mV (10 mA cm^{-2}), 480□510 times than that of commercial IrO_2 catalyst. More importantly, the HN-Ir NC catalyst shows no evident deactivation after continuous 100 h OER operation in acidic medium.

Introduction

Polymer electrolyte membrane water electrolysis (PEMEC) is viewed as a clean and promising way to convert electrical energy to hydrogen, playing an important role in modern sustainable energy conversion and storage devices.[1-3] Due to the sluggish oxygen evolution reaction (OER) kinetics and harsh acidic environment, the electrode of PEMEC should be catalytically active and highly stable under operating conditions.[3-5] Currently, iridium-based metal oxides, such as IrO_2, have been widely used in water electrolysis.[6,7] Unfortunately, IrO_2 still tends to decompose in strong acidic media ascribed to the loss of active surface area and the changes of iridium species oxidation state under a prolonged operating condition.[8,9] Although significant efforts have been devoted to developing various acidic catalysts, the corresponding catalytic mechanisms are still unclear attributed to the complex dynamic reaction system.[10,11] Furthermore, most of operando-tested electrodes are fabricated by simply casting catalyst powder onto substrates with only physical contact, and the detached sample of electrode would affect the signal of operando experiment leading to inauthentic dynamic evolution under OER conditions. Therefore, the development of highly acidic-resistance OER electrocatalysts with an excellent catalytic activity and a stable electrode configuration from the aspect of mechanistic understanding is much anticipated for practical PEMEC applications but remains a considerable challenge. To this end, an atomic-level identification of the nature of the active site under working conditions is imperative to design efficient acidic-resistance OER catalysts.

Up to now, enormous efforts have been paid to improve acidic-OER catalysts, such as transition metal substitution, structural engineering, element doping and so on (Co-RuIr, Ir_xCu, $IrO_x/SrIrO_3$, Ir-STO).[12-15]

However, the easy changes in the oxidation state of the Ir-based sample would cause continuous dissolution of active metal attributed to the presence of manifold Ir-O coordination.[9] Recently, downsizing the expensive IrO_x to single-atom iridium provides an efficient pathway to create cost-efficient catalyst and improve its activity and stability because of the strong metal-support interaction.[16] The catalytic activity and stability of single-atom catalysts are highly dependent on the local coordination structure of metal sites, directly related to the interaction between electrons and the geometric structure. The strong metal-support interactions can facilitate large electrons transfer from the metal to neighboring atoms towards high acidic-OER activity. Although various M-N_x moieties have been achieved in single-atom catalysts towards efficient electrocatalytic reaction,[17-19] inadequate electronic structure activation and unreliable atomic configuration limit the potential of M-N-C catalysts for high efficiency and stable acidic water oxidation.[20,21] Hence, it is urgently necessary to find an effective way to activate the acidic OER activity and improve the dissolution resistance of ultra-low iridium catalysts via a strong electron coupling between the single-atom active sites and their single-atom anchoring substrate.[22] Moreover, it has been reported that the structure of single-atom catalysts is easily reconstructed to a higher valence state for faster adsorption of reactants to achieve efficient activity in catalytic reactions. This means that the electronic structure of the active center can be dynamically manipulated at low voltages to significantly improve the catalytic activity. Therefore, for the single-atom centers embedded into 3D conductive substrate with stable active sites configuration, in-depth understanding of the reaction dynamics of active catalytic center at the atomic scale can provide new insights into the design of acidic-OER catalysts.

Here, to realize high catalytic activity and long-time durability in acidic medium, we design a new type of single-atomic Ir sites coupling in heterogeneous nitrogen-configured 3D substrate (HN-Ir NC) as ultralow-iridium electrocatalysts via a controllable and novel “electric-driven amino-induced” strategy. At atomic level, the active hetero-Ir-N_4 moieties were spatially confined in the 3D conductive carbon substrate with a strong interfacial chemical coupling owing to the selective ion-bonding effect in the weak redox units of the PAni and electric-driven NH_2 (Figure 1a). Interestingly, the *operando* synchrotron radiation X-ray absorption fine structure (XAFS) spectroscopy reveals that an oxygen was dynamically pre-adsorbed on the Ir site in the form of O-hetero-Ir-N_4 moiety under low driven-potential, which accelerates the transfer of electrons from the metal sites to neighboring atoms under the oxygen traction towards faster reaction kinetics. More importantly, the *operando* synchrotron radiation infrared (SRIR) and electrochemical impedance spectroscopy (EIS) directly observed H_2O adsorption under low driven voltage and crucial $^*OOH$ intermediate production on the active O-hetero-Ir-N_4 sites because of electrophilic effect of dynamic-coupling oxygen during the acidic-OER process, quickly overcoming the rate-determining step of water oxidation and then boosting an efficient acidic-OER activity and stability. As a result, the developed HN-Ir NC delivers low overpotential of 216 mV to achieve a current density of 10 mA cm^{-2} for acidic OER with an ultra-high mass activity of 2860 A g_{metal}^{-1}, and a huge turnover frequency (TOF) of 5110 h^{-1}, ~480 and 510 times than that of commercial IrO_2 catalyst (6 A g^{-1}, 10 h^{-1}), which endows HN-Ir NC as the best acidic-OER electrocatalyst based on the mass activity reported so far. Furthermore, the HN-Ir NC catalyst

could show ~97% Faradaic efficiency for OER and have no obvious attenuation of essential acidic-OER activity in the continuous operation of 100 h in acidic medium.

Results And Discussion

Structure characterization of HN-Ir NC. The ultra-low-iridium electrocatalyst with atomically-dispersed Ir sites coupling in the heterogeneous nitrogen-configured 3D substrate (HN-Ir NC) was synthesized via a controllable and novel “electric-driven amino-induced” strategy. The polyaniline layer with plenty of surface reductive benzenoid-amine groups was first electrodeposited onto a 3D carbon substrate, and then functionalized with amino groups by mild heat treatment in ammonia solution. It is noted that the surface reductive benzenoid-amine groups and -NH_2-derived uncoordinated N site act as the anchoring sites for Ir atoms during ions exchange and pyrolysis processes. Notably, the ultra-low-iridium atoms were chemically coupled with N sites on the 3D substrate to form the active and stable HN-Ir NC catalyst. The obtained HN-Ir NC catalyst can be verified by the scanning electron microscopy (SEM, Supplementary Figs. 1, 2, 3) and transmission electron microscopy (TEM, Supplementary Fig. 4). The SEM and TEM images (Figure 1b and c) clearly show that the atomically dispersed Ir atoms chemically coupled onto 3D layered carbon substrate, with no noticeable metal particles observed. In particular, high-angle annular dark-field scanning transmission electron microscopy (HAADF-STEM) further confirmed that Ir was in the form of a single atom riveted on the carbon surface with a particle size of ~2.3 nm (Supplementary Fig. 5). The elemental mappings (Figure 1d) indicate the uniform distribution of C, N and Ir in the selected carbon fibre area. Similarly, the coupled plasma optical emission spectrometry (ICP-OES) characterizations reveal the existence of Ir in the obtained HN-Ir NC with an ultra-low content about 3.5 μg cm^{-2}. X-ray diffraction results (Supplementary Fig. 6) further proved that no Ir nanoparticles and clusters were observed for HN-Ir NC, indicating a uniform dispersion of Ir sites throughout the 3D substrate.

To determine the local structure of Ir at the atomic scale, the X-ray absorption near edge spectroscopy (XANES) of C and N *K*-edges were collected. The C *K*-edge spectra of PAni-800 ˚C in Figure 2a shows two obvious peaks located at 285.4 and 288.7 eV can be assigned to the 1s→2p excitation of C-C π^* and C-N_2, respectively.[23] After Ir sites coupling onto NC substrate, a new peak was observed at 287.8 eV that can be attributed to the excitation of C-N_1, suggesting the presence of hetero-nitrogen after ammonia water treatment. The N *K*-edge in Figure 2b, the peaks of excitation of C-N and hetero-Ir-N were obtained. The high-energy shift of C-N reveals that the introduction of amino-derived N results in an electron transfer between C and N. Above results clearly reveal the coordination of single-atomic Ir sites with hetero pyridinic- and amino-derived nitrogen in HN-Ir NC. Furthermore, the five fitting peaks of 406.3, 401.2, 400.1, 399.7, 398.9 and 398.4 eV in N 1s XPS spectra (Figure 2c) can be assigned to N-O, graphitic N, pyrrolic N, Ir-N, Ir-amino-N and pyridinic N, respectively.[24,25] This further clearly demonstrates the formation of heterogeneous N configured with Ir sites for HN-Ir NC. Moreover, the Ir 4f XPS spectra clearly reveals that high-valence Ir is coupled onto 3D substrate in the form of Ir^{3+} with hetero-N configuration (Figure 2d).[26] The atomic structure configuration of Ir site was obtained by the measurements of Ir L_3-edge XAFS spectra. As seen from XANES of Ir L_3-edge in Figure 2e, it can be inferred that the high-valence

Ir forms the coordination structure of Ir-N based on the position of the absorption edge and the oscillation frequency. Figure 2f shows one peak located at ~1.6 Å that can be assigned to the Ir-N coordination.[27] To further quantify the local coordination structure of Ir, the EXAFS of Ir was additionally fitted. The fitted results in Supplementary Table 1 show that the coordination number is close to 4 with two short and two long bonds, consisting of Ir-N_1 (1.92 Å) and Ir-N_2 (1.95 Å) and suggesting the hetero-N configuration of atomic-dispersed Ir sites. Therefore, above results clearly verify the formation of hetero-Ir-N_4 moieties coupled onto 3D substrate by coordinating Ir sites with hetero-N ligand for the HN-Ir NC catalyst.

OER performance of HN-Ir NC catalyst. The electrocatalytic OER activities of HN-Ir NC were performed in 0.5 M H_2SO_4 with a three-electrode system, along with PAni-Ir-800˚C, Ir nanoparticle loading NC catalyst (Ir-NP/NC) and commercial IrO_2 for comparison. Figure 3a shows the linear sweep voltammetry (LSV) curves for the HN-Ir NC and the reference samples. Dramatically, the HN-Ir NC exhibits the most excellent acidic-OER activity, only requiring ultra-low overpotentials of 216 and 292 mV to achieve water oxidation current density of 10 and 100 mA cm^{-2}, respectively. In contrast, as shown in Figure 3b, the PAni-Ir-800 ˚C and commercial IrO_2 display insufficient acidic-OER activity (320, 412 and 300, 385 mV, respectively, Supplementary Fig. 8), suggesting hetero-nitrogen- configured Ir sites to achieve efficient water oxidation activity in acidic medium by functionalization of polyaniline and amino groups. Importantly, the electrochemically active surface area (ECSA) of HN-Ir NC was obtained by roughness factor (Supplementary Figs. 9, 10), and the specific activity of HN-Ir NC still surpasses PAni-Ir-800˚C and IrO_2 when normalizing the current density to per ECSA (Supplementary Figs. 11). Moreover, Figure 3c displays a smaller Tafel slope of 32 mV dec^{-1}, suggesting a faster OER kinetics and electron transfer occurred over Ir singles sites. Based on the Arrhenius plots results of Figure 3d, Supplementary Figs. 12 and 13, the activation energy of HN-Ir NC is downshifted to 26.56 KJ mol^{-1} relative to that of commercial IrO_2 (44.27 KJ mol^{-1}) under the overpotential of 216 mV, which further proves the faster OER kinetics after high-valence Ir single sites integrated onto the carbon substrate with the active hetero-N-coordination.

To further obtain the intrinsic activity of HN-Ir NC, the mass activity and TOF were calculated according to the active Ir sites (Figure 3e). It needs to be specially noted that the mass activity and TOF of HN-Ir NC are about 2860 A g_{metal}^{-1} and 5110 h^{-1} at a pretty small overpotential of 216 mV, ~480 and 510 times than that of commercial IrO_2 catalyst (6 A g^{-1}, 10 h^{-1}). Notably, the HN-Ir NC displays ultra-high mass activity of 10900 A g_{metal}^{-1} and TOF of 18900 h^{-1} at a representative overpotential of 260 mV. To the best of our knowledge, the mass activity of HN-Ir NC is the highest among the reported acidic-OER electrocatalysts (Supplementary Table 2). With the increase of overpotentials, the mass activity and TOF increase significantly, indicating faster OER catalytic kinetics. The details of the oxygen product quantification by gas chromatography are presented in Supplementary Fig. 14. It can be seen that the HN-Ir NC offers an excellent four-electron ($4e^-$) OER with Faradaic efficiencies of 95-98% under various potentials in acid medium. Thanks to the excellent acidic OER performance of HN-Ir NC, we have conducted the test of overall water splitting in a two-electrode configuration. The HN-Ir NC and commercial Pt/C were used as the anode and cathode, respectively. It can be drawn from Supplementary Fig. 15 that the input potential

of water splitting in practical electrolyzers is about 1.49 V for achieving the current density of 10 mA cm^{-2}, significantly superior to that of standard electrodes (Pt/C vs IrO_2, 1.58 V). The stability of catalyst is an important performance index for evaluating the real application potential, especially in harsh operating conditions. To assess the durability of HN-Ir NC and reference sample, a chronopotentiometry test at the current density of 10 mA cm^{-2} was performed. As shown in Figure 3f, essential acidic-OER activity has no apparent attenuation in continuous operation of 100 h for HN-Ir NC, obviously outperforming commercial IrO_2, which is attributed to the formation of hetero-Ir-N_4 moieties strongly coupled onto 3D substrate (Supplementary Figs.16, 17). It can efficiently avoid the repeated changes in the Ir oxidation state for faster water oxidation kinetics and strong acid-resistance.

Operando **EIS and SRIR analysis.** EIS is an effective electrochemical measurement method to obtain the adsorption and desorption kinetics information of the reactants on the electrode surface. To intuitively obtain the evolution of the reactive species H_2O or key intermediate $^*OOH$ on active sites, *operando* EIS tests were performed at different applied voltages to further understand the electrochemical reaction kinetics process.[28] As seen from the Nyquist plots in Figure 4a and b, the measured impedance of acidic-OER process on HN-Ir NC and PAni-Ir-800˚C were measured from open circuit potential (OCP, ~0.95 V) to 1.45 V. Through the direct changing trend and size of the semicircle in the Nyquist plots, faster kinetics and adsorption of reactants with the increase of voltage can be revealed. At the same time, HN-Ir NC shows faster reaction kinetics which is attributed to the active hetero-Ir-N_4 coordination and the strong coupling substrate effect. Importantly, these Nyquist plots should first need to be fitted by equivalent circuit diagrams to access to the key fitting parameters R_{CT} and C_{DL} (Supplementary Fig. 18). R_{CT} and C_{DL} can be used to represent the $H_2O/^*OOH$ ions adsorption resistance and pseudocapacitance on the catalyst surface. It can be seen from the changes of fitting results for R_{ct} in Figure 4c, the R_{ct} of HN-Ir NC is lower than that of PAni-Ir-800 ˚C, suggesting a faster adsorption kinetics of key intermediates $^*OOH$ during acidic OER process (Supplementary Table 3, 4). Notably, the R_{ct} decreases faster than that of PAni-Ir-800˚C within 1.1 V, which further reveals that oxygen-species are rapidly adsorbed at lower driven-voltages to produce key intermediates $^*OOH$ accumulated over the active hetero-Ir-N_4 moieties.

To effectively identify the reaction intermediates and access to the catalytic reaction mechanism, *operando* SRIR measurements, which is highly sensitive to oxygen-containing intermediates, was performed with a home-made electrochemical SRIR cell.[29,30] The SRIR results of HN-Ir NC were obtained at different applied voltages in Figure 4d. A new absorption band at 784 cm^{-1} was observed for HN-Ir NC at potential of 1.25 V, which can be assigned to the emergence of Ir-O during OER process.[31] This indicates a structural self-optimization of Ir site under low driven-potential to form the active structure O-hetero-Ir-N_4 by an oxygen adsorption. The intensity of vibration absorption shows a positive correlation with the further increase of applied-potentials and remain unchanged when the potential exceeds 1.35 V. It is noted that a new absorption band in the vibration frequency of 1055 cm^{-1} was observed for HN-Ir NC when potential > 1.35 V, which could be attributed to the emergence of crucial intermediate $^*O\text{-}OH$ during acidic-OER process.[30] In comparison, *operando* SRIR measurements were performed for PAni-Ir-800˚C at

typical voltages of 1.30 V (representing initial potential) and 1.45 V (representing reaction potential). Figure 4e shows that no obvious absorption bands were observed in the vibration frequencies of 1300-600 cm^{-1} for PAni-Ir-800˚C under potential of 1.45 V (Supplementary Figs.19). This phenomenon indicates that high-valence Ir sites coupled onto 3D substrate with hetero-N configuration by strong coupling substrate effect can pre-adsorb an oxygen to form stable and highly active O-hetero-Ir-N_4 structure, obviously accelerating the 4-electron kinetics process and promoting the formation of key OER reaction intermediates. To clarify the dynamic relationships between Ir-O and intermediates *OOH, the peak intensity enhancements of the absorption bands at 784 and 1055 cm^{-1} were plotted as a function of applied potential in Figure 4f. Notably, along with the increased applied potentials, the vibration band intensity of key *OOH for HN-Ir NC catalyst increases obviously higher than that of PAni-Ir-800˚C. Most importantly, the dynamic-coupling of oxygen occurs at 1.25 V, clearly before the appearance of the new vibration band of key *OOH for HN-Ir NC during OER working conditions. Above results clearly reveal that the potential-driven dynamic-coupling of oxygen over the Ir single sites was observed, which would in turn evidently promote the generation of the key *OOH intermediates over the O-hetero-Ir-N_4 moieties towards an efficient and fast $4e^-$ OER process in acidic medium.

***Operando* XAFS analysis.** To further access to the evolutionary nature of the active Ir single sites under working conditions, *operando* XAFS measurement (Supplementary Fig. 20) was carried out in a home-made cell by using three-electrode standard electrochemical workstation.[32] The XANES spectra under different potentials in Figure 5a show that the intensity of white-line of HN-Ir NC increases gradually with the increase of voltage, accompanied by a slight positive-shift. This indicates that more electron vacant states of Ir sites were observed under voltage-driven, where more electrons move from Ir to nearby atoms and adsorb oxygen-species to active electronic surface states of Ir centers. This result suggests that the traction of pre-adsorbed-oxygen on the Ir site under potential-driven obviously optimized the electronic structure of hetero-Ir-N_4 moieties for faster reaction kinetics. To further clarify the evolution of the local coordination structure of Ir sites under applied potential, the FT Ir-L_3 edge EXAFS were shown in Figure 5b, where a dominant peak of ~1.6 Å can be attributed to the coordination structure of metallic and non-metallic bonding (Ir-N/O). Interestingly, the peak intensity increased significantly at potential of 1.25 V and further enhanced with increased potential applied onto the electrode, suggesting a local structural self-optimization and adsorption of reactive species under OER working conditions. Quantitatively, the Ir L_3-edge EXAFS fitting results (Figure 5c, Supplementary Fig. 21 and Table 5) clearly show an additional Ir-O coordination with the bond length of 2.06 Å at applied potential of 1.25 V. This result further proves that an oxygen was dynamically coupled on the Ir site in form of O-hetero-Ir-N_4 moiety with coordination number of N=5 (two short Ir-N bonds, two long Ir-N bonds and one Ir-O bond). With applied potential increasing to 1.35 V, a new Ir-O bond was observed over the active O-hetero-Ir-N_4 moieties with coordination number of 2 for Ir-O bond. This indicates that oxygen adsorbed onto Ir sites can promote the adsorption of the reactive oxygen-species under significant electrophilic effect of dynamic-coupling oxygen. With a further increase in the bias potential to 1.45 V, the peak intensity shows a slight increase accompanied by contraction of Ir-O bond, indicating the deprotonation of adsorbed oxygen-species into

the key *OOH intermediates on the activated O-hetero-Ir-N_4 moieties by electrophilic effect, which is consistent with the *operando* SRIR results. The *operando* SRIR and XAFS results jointly reveal that a potential-driven dynamic oxygen-coupling was achieved under OER working conditions, which promotes the generation of key *OOH intermediates and then accelerates the four-electron reaction kinetics towards an efficient OER in acidic environments (Figure 5d).

Discussion

In summary, a highly-efficient and durable single-atomic HN-Ir NC catalyst with strong coupling hetero-Ir-N_4 moieties was developed by a controllable and novel “electric-driven amino-induced” strategy. Dynamic mechanism studies by using the advanced *operando* XAFS and SRIR techniques indicated that an oxygen is dynamically coupled onto the Ir site and then a key *OOH is produced by the electrophilic effect of dynamic-coupling oxygen over O-hetero-Ir-N_4 moieties under working potentials, which greatly accelerates the 4-electron reaction kinetics towards an efficient acidic-OER activity and stability. The as-obtained single-atomic HN-Ir NC catalyst delivers an ultra-low overpotential of 216 mV at 10 mA cm^{-2}, reaching an ultra-high mass activity of 2860 A g^{-1} and a huge turnover frequency (TOF) of 5110 h^{-1}, which endows HN-Ir NC as the best acidic-OER electrocatalyst based on the mass activity and TOF reported so far. Hence, this discovery of active sites evolution under working conditions can provide a coordination-engineered strategy for designing advanced acidic-OER electrocatalysts.

Methods

Synthesis of the HN-Ir NC. The HN-Ir NC was fabricated in typical three well-designed steps, consist of surface functionalization of 3D carbon paper, surface amino-treatment and ion-exchange, high-temperature pyrolysis. Firstly, the 3D carbon paper is activated and cleaned by calcining it at 500℃ under air for 2h, and then washed with concentrated nitric acid and deionized water. Next, the polyaniline is electrodeposited on the 3D substrate in a three-electrode system. Specifically, pre-treated carbon paper, carbon rod, and saturated calomel electrode (SCE) were employed as working, counter, and referenced electrodes respectively, and a mixed solution of aniline (10 ml), concentrated nitric acid (12 ml) and deionized water (78 ml) was used as electrolyte. The working electrode was first subjected to anodic treatment at an oxidative constant voltage of 0.7 V (SCE) for 400 s to allow full polymerization of aniline molecules on electrode surface, and then was switched to a reductive constant voltage of -0.3 V (SCE) to tune the ratio of quinonoid- and benzenoid-amine groups in surface polyaniline layer for compete surface adsorption of NO_3^-. Subsequently, the obtained substrate was intruded into concentrated ammonia water for hydrothermal treatment for 5h at 90˚C. Afterwards, the functionalized carbon substrate was immersed in a 60 ml aqueous solution containing H_2IrCl_4 (0.06 mmol/L) at 70 °C under continuous stirring for 2 h, where an anion exchange between $[IrCl4]^{2-}$ and pre-adsorbed NO_3^- as well as $[IrCl4]^{2-}$ adsorption over the amino group were realized on the surface polyaniline layer of carbon substrate. The surface benzenoid-amine and amino groups in surface polyaniline can easily couple with Ir complex ions, firmly anchoring Ir ions with heterogeneous nitrogen on the surface of carbon paper. Finally, the obtained

3D carbon paper with rich Ir atoms was transferred to a tubular furnace for high temperature annealing in an argon atmosphere, where the furnace was maintained at 800°C for 3h to obtained the HN-Ir NC catalyst.

Synthesis of the PAni-Ir-800°C. The general process of synthesis is similar to that of the preparation of HN-Ir NC. It is noted that in the process of substrate surface functionalization, PAni was not treated with concentrated ammonia water, and the final catalyst did not form hetero-nitrogen coordination and it was called PAni-Ir-800°C.

Synthesis of Ir-NP/NC. The general process of synthesis is similar to that of the preparation of PAni-Ir-800°C. It is noted that in the process of the adsorption of Ir precursor, it is necessary to increase the metal feeding amount to 0.18 mmol/L, and then the carbonization temperature was increased to 1000°C. The obvious Ir nanoparticles were obtained over the 3D carbon paper and it was called Ir-NP/NC.

Calculation of Roughness Factor (RF)

The roughness factor (RF) is calculated by taking the estimated ECSA and dividing by the geometric area of the electrode, 2.0 cm^2. And according to the equation:

$RF = ECSA/S_{geo.}$

The ECSA of the catalyst sample is calculated from the double layer capacitance according to equation:

$ECSA = C_{dl}/C_s$

Where C_s is the specific capacitance of the sample, and it have been measured for a variety of electrode in acidic solution and typical value reported range between C_s = 0.015-0.110 mF cm^{-2} in H_2SO_4. Hence, we use general specific capacitances of C_s = 0.035 mF cm^{-2} based on typical reported value. The double-layer charging can be measured via CVs, a potential range in which no apparent Faradaic processes occur was determined from static CV. This range is typically a 0.1 V potential window (0.6~0.7 V vs. SCE) centered at the open-circuit potential of the system.

Another activity metric sometimes reported in the electrocata mF cm^{-2} mF cm^{-2}lysis literature is the specific activity at a given overpotential. The definition of specific activity refer to the specific current density per ECSA (J_{ECSA}), which is calculated by dividing the current density per geometric area ($J_{geo.}$) by the RF at a given overpotential and according the equation:

$J_{ECSA} = J_{geo.}/RF$

Turnover frequency (TOF) and Mass activity calculations.

$$TOF = \frac{the\ measured\ current\ density\ j * NA * 10^3}{4 * F * surface\ active\ sites\ (mol)}$$

F represents Faraday constant (96485 c cm^{-1}). NA represents Avogadro constant ($6.02*10^{23}$) We estimated the number of the active sites as the total number of the surface sites of Ir for the catalysts, which might underestimate the real TOF.

Mass activity (A g_{metal}^{-1}) values were calculated from the electrocatalyst loading *m* and the measured current density *j* at overpotential of 216 and 260 mV:

$$Mass\ activity = \frac{j}{m}$$

Operando **EIS measurements.** *Operando* characterization tandem electrochemical operation were carried out specify potential for 10 min to obtain the surface chemical composition and structural information of materials. EIS tests were performed at different potentials in the frequency range of 0.01-100000 Hz.

Operando **SRIR measurements.** *Operando* SRIR measurements were performed at the infrared beamline BL01B of the National Synchrotron Radiation Laboratory (NSRL, China) by using home-made top-plate cell, which the infrared transmission window of cell is made of ZnSe crystal with low light absorption (cut-off energy of ~625 cm^{-1}). The synchrotron radiation IR testing device consists of two carefully-designed parts, including an IR spectrometer (Bruker 66 v/s) with a KBr beam splitter and various detectors (herein, a liquid-nitrogen-cooled MCT detector was used) and an IR microscope (Bruker Hyperion 3000) with a 16x objective, which can provide infrared spectroscopy measurements over a broad range of 15–4000 cm^{-1} and a high spectral resolution of 0.25 cm^{-1}. Attentively, during the *operando* SRIR measurement, infrared signal is very sensitive to water molecules and is easily disturbed. By pressing the electrode and window to control the thickness of the water film in the micron-scale, the infrared signal-to-noise ratio (SNR) is improved. To obtain the information of catalyst surface and further improve the signal quality of SRIR spectra under working condition, the reflection mode of infrared light with vertical incidence is adopted in the test. Bedsides, each high-resolution infrared absorption spectrum with resolution of 2 cm^{-1} was obtained by averaging 514 scans. To avoid the signal difference caused by sample falling off, a constant potential was applied to the catalyst electrode for 20 min, and then all infrared spectral acquisitions were carried. The background spectrum of the catalyst electrode was acquired at an open-circuit voltage before each systemic OER measurement, and the measured potential ranges of the OER were 1.0–1.42 V. Noticeably, in order to show a higher signal-to-noise ratio of the data, the curves were smoothed through 100 points in the later stage of data processing.

Operando **XAFS measurements.** The *operando* XAFS measurements of Ir L_3-edge were carried out at the 1W1B station in the Beijing Synchrotron Radiation Facility (BSRF), China. The storage ring of BSRF was operated at 2.5 GeV with a maximum current of 250 mA. The beam from the bending magnet was

monochromatized utilizing a Si (111) double-crystal monochromator and further detuning of 15% to remove higher harmonics. The electrochemical operando XAFS tests were performed by home-made cell in 0.5 M H_2SO_4 electroyte. The XAFS spectra were collected through the fluorescence mode with 19-element solid state detector. The HN-Ir NC catalyst on the 3D carbon paper was cut into 1*2 cm^2 and then sealed in a cell by Kapton film. In order to obtain the dynamic evolution information of the active site during the electrochemical reaction, a series of representative voltages (1.25~1.45 V) were applied to the electrode. During the collection of XAFS measurements, the position of the absorption edge (E_0) was calibrated using standard sample of Ir, and all XAFS data were collected during one period of beam time.

Declarations

Data availability

All the data reported in this paper are available from the corresponding author upon request.

Acknowledgements

This work was supported by the National Key Research and Development Program of China (2017YFA0402800), the National Natural Science Foundation of China (Grants No. U1932212, U1932109, 11875257), the Postdoctoral Science Foundation of China (2020M682042).

Author contributions

S.Q.W., Q.H.L. and H.S. conceived the project. Q.H.L. and H.S. designed the *operando* SRIR and XAFS experiments. H.S. and W.L.Z. carried out the experiments. S.Q.W., Z.M.Q., L.R.Z., H.Z., Y.L.L., M. H.L., X.X.Z., X.S., Y.Z.X., F.C.H., J.Z., and T.D.H. analyzed the experimental data. The manuscript was written by S.Q.W., Q.H.L. and H.S. with contributions from all authors.

Competing interests: The authors declare no competing financial interests.

Additional information

Supplementary information is available for this paper.

Correspondence and requests for materials should be addressed to S.Q.W. or Q.H.L.

Reprints and permissions information is available at www.nature.com/reprints.

Publisher's note: Springer Nature remains neutral with regard to jurisdictional claims in published maps and institutional affiliations.

References

1 Chu, S. & Majumdar, A. Opportunities and challenges for a sustainable energy future. *Nature* **488**, 294-303 (2012).

2 Yin, Q. *et al.* A fast soluble carbon-free molecular water oxidation catalyst based on abundant metals. *Science* **328**, 342-345 (2010).

3 Jiao, Y., Zheng, Y., Jaroniec, M. & Qiao, S. Z. Design of electrocatalysts for oxygen-and hydrogen-involving energy conversion reactions. *Chem. Soc. Rev.* **44**, 2060-2086 (2015).

4 Spoeri, C., Kwan, J. T. H., Bonakdarpour, A., Wilkinson, D. P. & Strasser, P. The stability challenges of oxygen evolving catalysts: towards a common fundamental understanding and mitigation of catalyst degradation. *Angew. Chem. In. Ed.* **56**, 5994-6021 (2017).

5 Lee, Y., Suntivich, J., May, K. J., Perry, E. E. & Shao-Horn, Y. Synthesis and activities of rutile IrO2 and RuO2 nanoparticles for oxygen evolution in acid and alkaline solutions. *J. Phys. Chem. Lett.* **3**, 399-404 (2012).

6 Kim, J. *et al.* High-performance pyrochlore-type yttrium ruthenate electrocatalyst for oxygen evolution reaction in acidic media. *J. Am. Chem. Soc.* **139**, 12076-12083 (2017).

7 Yang, L. *et al.* Efficient oxygen evolution electrocatalysis in acid by a perovskite with face-sharing IrO 6 octahedral dimers. *Nat. Commun.* **9**, 1-9 (2018).

8 Zhang, R. *et al.* A Dissolution/Precipitation Equilibrium on the Surface of Iridium-Based Perovskites Controls Their Activity as Oxygen Evolution Reaction Catalysts in Acidic Media. *Angew. Chem. In. Ed.* **58**, 4571-4575 (2019).

9 Povia, M. *et al.* Operando X-ray characterization of high surface area iridium oxides to decouple their activity losses for the oxygen evolution reaction. *Energy Environ. Sci.* **12**, 3038-3052 (2019).

10 Moysiadou, A., Lee, S., Hsu, C.-S., Chen, H. M. & Hu, X. Mechanism of Oxygen Evolution Catalyzed by Cobalt Oxyhydroxide: Cobalt Superoxide Species as a Key Intermediate and Dioxygen Release as a Rate-Determining Step. *J. Am. Chem. Soc.* **142**, 11901-11914 (2020).

11 Wu, T. *et al.* Iron-facilitated dynamic active-site generation on spinel CoAl 2 O 4 with self-termination of surface reconstruction for water oxidation. *Nat. Catal.* **2**, 763-772 (2019).

12 Shan, J., Ling, T., Davey, K., Zheng, Y. & Qiao, S. Z. Transition-metal-doped RuIr bifunctional nanocrystals for overall water splitting in acidic environments. *Adv. Mater.* **31**, 1900510 (2019).

13 Shi, Q. *et al.* Nanovoid incorporated IrxCu metallic aerogels for oxygen evolution reaction catalysis. *ACS Energy Lett.* **3**, 2038-2044 (2018).

14 Seitz, L. C. *et al.* A highly active and stable IrOx/$SrIrO_3$ catalyst for the oxygen evolution reaction. *Science* **353**, 1011-1014 (2016).

15 Liang, X. *et al.* Activating inert, nonprecious perovskites with iridium dopants for efficient oxygen evolution reaction under acidic conditions. *Angew. Chem. In. Ed.* **58**, 7631-7635 (2019).

16 Wang, Q. *et al.* Ultrahigh-loading of Ir single atoms on NiO matrix to dramatically enhance oxygen evolution reaction. *J. Am. Chem. Soc.* **142**, 7425-7433 (2020).

17 Li, B. *et al.* Mussel-inspired one-pot synthesis of transition metal and nitrogen co-doped carbon (M/N–C) as efficient oxygen catalysts for Zn-air batteries. *Nanoscale* **8**, 5067-5075 (2016).

18 Teng, Y. *et al.* Atomically Thin Defect-Rich Fe–Mn–O Hybrid Nanosheets as High Efficient Electrocatalyst for Water Oxidation. *Adv. Fun. Mater.* **28**, 1802463 (2018).

19 Liu, L., Su, H., Tang, F., Zhao, X. & Liu, Q. Confined organometallic Au1Nx single-site as an efficient bifunctional oxygen electrocatalyst. *Nano Energy* **46**, 110-116 (2018).

20 Zhao, M. *et al.* Metal–organic frameworks as selectivity regulators for hydrogenation reactions. *Nature* **539**, 76-80 (2016).

21 Imayoshi, R., Nakajima, K., Takaya, J., Iwasawa, N. & Nishibayashi, Y. Synthesis and Reactivity of Iron–and Cobalt–Dinitrogen Complexes Bearing PSiP-Type Pincer Ligands toward Nitrogen Fixation. *Eur. J. Inorg. Chem.* **2017**, 3769-3778 (2017).

22 Grimaud, A. *et al.* Activating lattice oxygen redox reactions in metal oxides to catalyse oxygen evolution. *Nat. Chem.* **9**, 457-465 (2017).

23 Liang, Y. *et al.* Covalent hybrid of spinel manganese–cobalt oxide and graphene as advanced oxygen reduction electrocatalysts. *J. Am. Chem. Soc.* **134**, 3517-3523 (2012).

24 Leinweber, P. *et al.* Nitrogen K-edge XANES–an overview of reference compounds used to identifyunknown'organic nitrogen in environmental samples. *J. Synchrotron Radita.* **14**, 500-511 (2007).

25 Yi, J.-D. *et al.* Atomically dispersed iron–nitrogen active sites within porphyrinic triazine-based frameworks for oxygen reduction reaction in both alkaline and acidic media. *ACS Energy Lett.* **3**, 883-889 (2018).

26 Jin, R. *et al.* Low temperature oxidation of ethane to oxygenates by oxygen over iridium-cluster catalysts. *J. Am. Chem. Soc.* **141**, 18921-18925 (2019).

27 Xiao, M. *et al.* A single-atom iridium heterogeneous catalyst in oxygen reduction reaction. *Angew. Chem.* **131**, 9742-9747 (2019).

28 Zhou, W. *et al.* Self-synergistic cobalt catalysts with symbiotic metal single-atoms and nanoparticles for efficient oxygen reduction. *J. Mater. Chem. A* **9**, 1127-1133 (2021).

29 Su, H. *et al.* Dynamic Evolution of Solid-Liquid Electrochemical Interfaces over Single-Atom Active Sites. *J. Am. Chem. Soc.* (2020).

30 Cheng, W. *et al.* Lattice-strained metal–organic-framework arrays for bifunctional oxygen electrocatalysis. *Nat. Energy* **4**, 115-122 (2019).

31 Zandi, O. & Hamann, T. W. Determination of photoelectrochemical water oxidation intermediates on haematite electrode surfaces using operando infrared spectroscopy. *Nat. Chem.* **8**, 778-783 (2016).

32 Fang, S. *et al.* Uncovering near-free platinum single-atom dynamics during electrochemical hydrogen evolution reaction. *Nat. Commun.* **11**, 1-8 (2020).

Figures

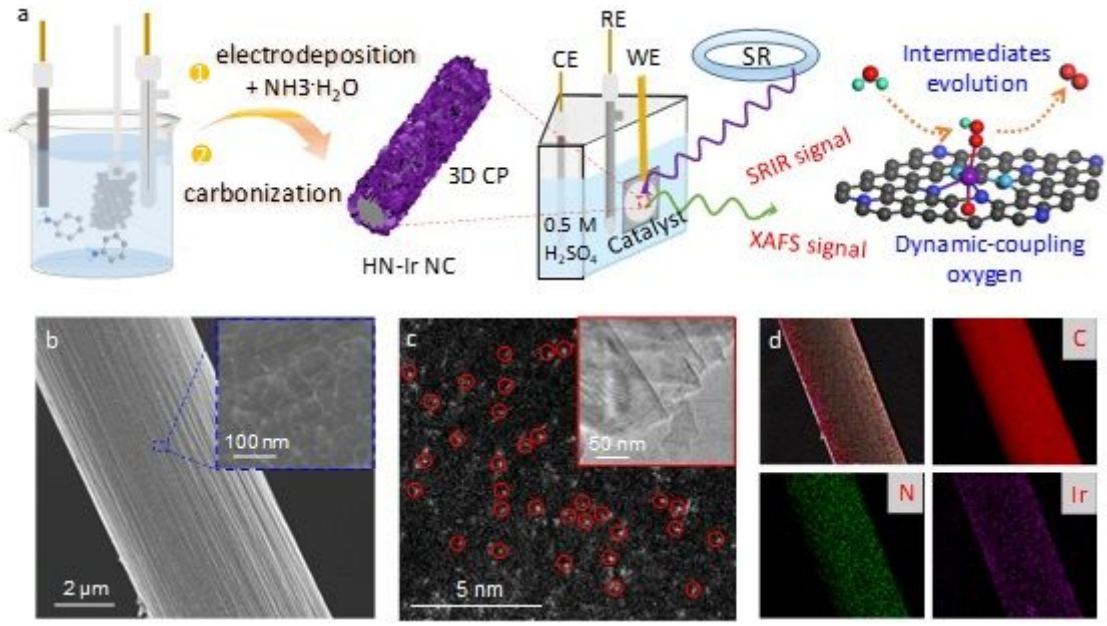

Figure 1

(a) Scheme of synthetic process. (b) SEM image of HN-Ir NC and the inset is a partially enlarged image. (c) HAADF-TEM image and the inset is TEM image. (d) STEM-EDS mapping images for HN-Ir NC.

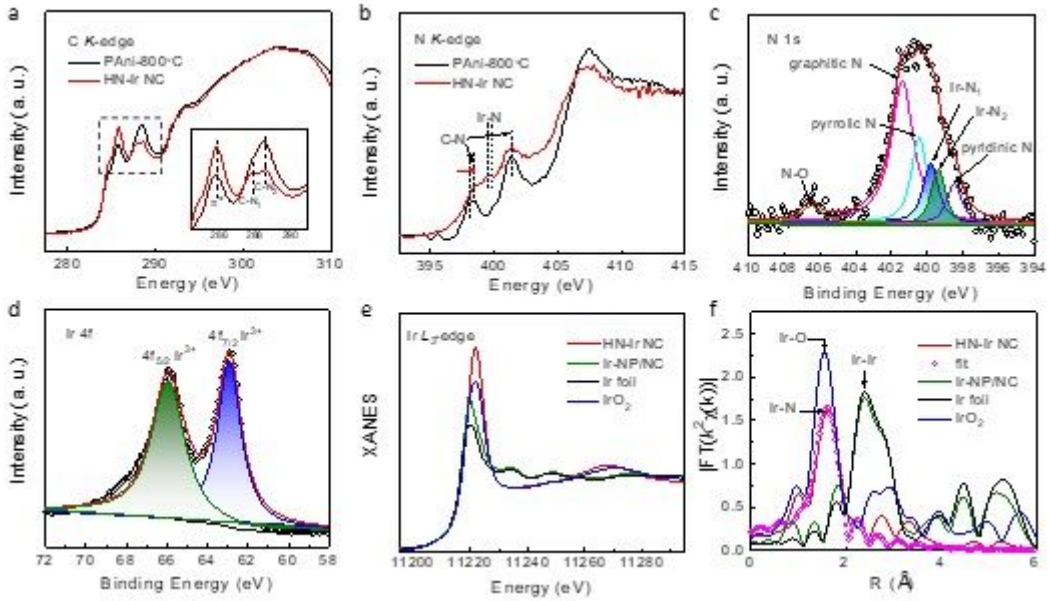

Figure 2

(a) C and (b) N K-edge XANES spectra of PAni-800 ˚C and HN-Ir NC. (c) N 1s and (d) Ir 4f XPS spectra of HN-Ir NC. (e) Ir L3-edge XANES spectra and (f) Fourier transforms (FTs) of the Ir L3-edge EXAFS oscillations of HN-Ir NC, Ir-NP/NC, Ir foil, IrO2, and the fitting curves of k2-weighted EXAFS spectra of HN-Ir NC.

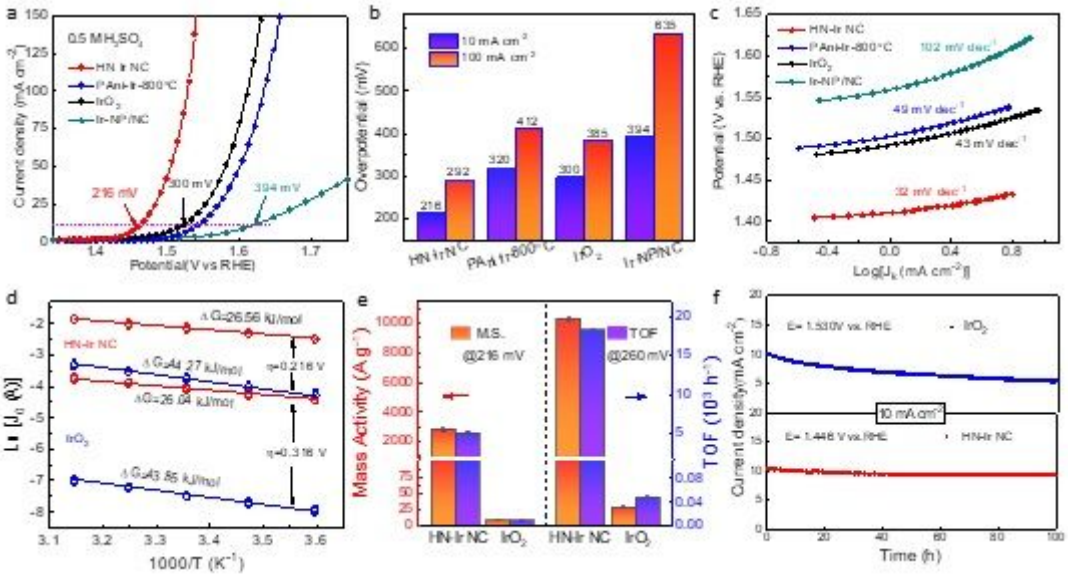

Figure 3

(a) Linear sweep voltammetry (LSV) curves, (b) overpotentials at 10 and 100 mA cm-2 and (c) Tafel slopes for HN-Ir NC, PAni-Ir-800 ˚C, IrO2 and Ir-NP/NC. (d) Arrhenius plots of HN-Ir NC. (e) Mass activity (M.A.) and turnover frequency (TOF) at an overpotential of 216 and 260 mV for HN-Ir NC and IrO2. (f) OER stability for HN-Ir NC and IrO2 at applied potential of 1.446 and 1.530 V, respectively.

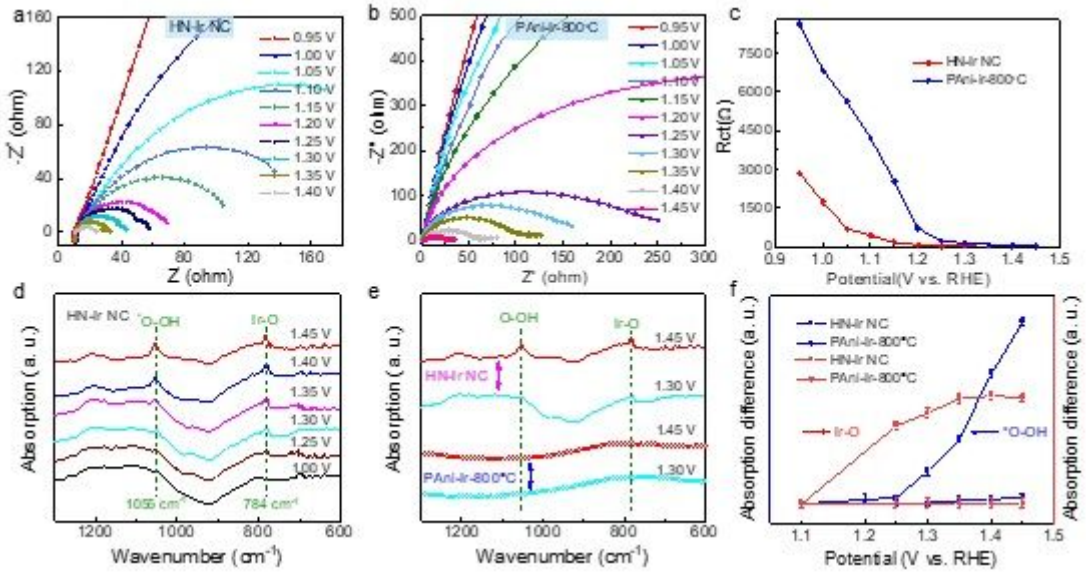

Figure 4

Nyquist plots for (a) HN-Ir NC and (b) PAni-Ir-800˚C catalysts at different applied potentials in 0.5 M H2SO4. (c) Response of the ions adsorption resistance (Rct) at different potentials for HN-Ir NC and PAni-Ir-800˚C. (d) Operando SRIR measurements in the range of 1300–600 cm-1 under various potentials for HN-Ir NC during the OER process. (e) SRIR results in the range of 1300–600 cm-1 at typical potentials of 1.30 and 1.45 V for HN-Ir NC and PAni-Ir-800˚C. (f) Intensity difference of infrared signals at 1055 and 784 cm-1 versus potentials for HN-Ir NC and PAni-Ir-800˚C during OER process.

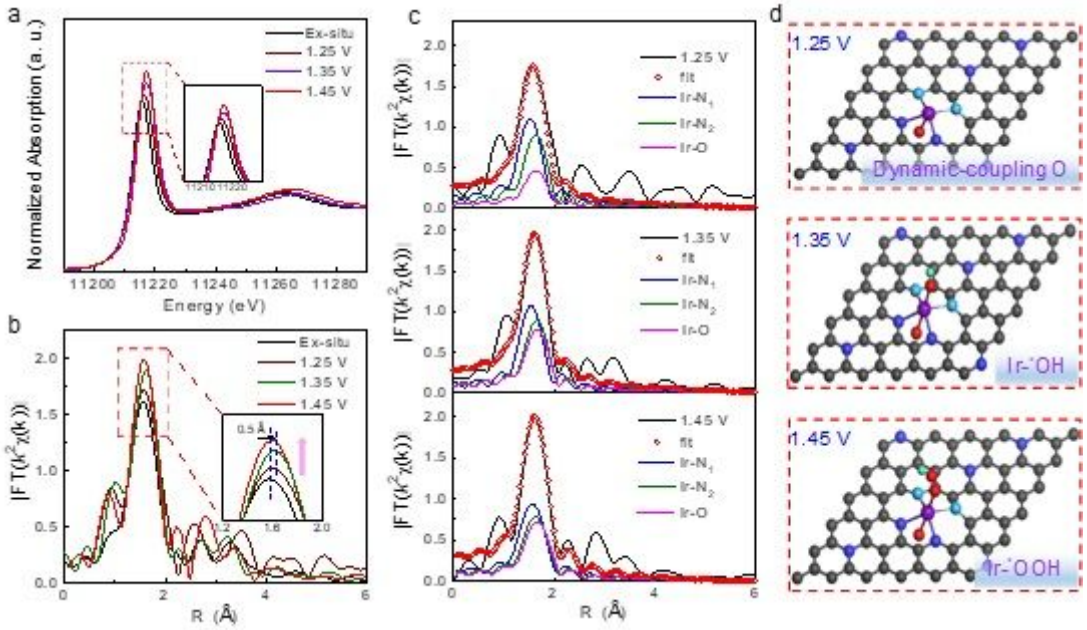

Figure 5

Operando XAFS measurement. (a) Operando XANES spectra recorded at Ir L3-edge of HN-Ir NC at different applied potentials from the 1.25 to 1.45 V during OER process. (b) Corresponding k2-weighted

Fourier transform (FT) spectra. (c) The fitting results recorded at Ir L3-edge and (d) OER mechanism diagrams of HN-Ir NC at 1.25, 1.35 and 1.45 V.

Supplementary Files

This is a list of supplementary files associated with this preprint. Click to download.

- Supplementarymaterials.docx